A Photoelectron and TPEPICO Investigation of the Acetone Radical Cation

Emma E. Rennie, Anne-Marie Boulanger, and Paul M. Mayer*

Department of Chemistry, University of Ottawa, 10 Marie-Curie, Ottawa, Canada, K1N 6N5

David M. P. Holland and David A. Shaw

Daresbury Laboratory, Daresbury, Warrington, Cheshire, WA4 4AD, U.K.

Louise Cooper

Department of Chemistry, Heriot-Watt University, Riccarton, Edinburgh, EH14 4AS, U.K.

Larisa G. Shpinkova

Department of Nuclear Spectroscopy Methods, Institute of Nuclear Physics, Moscow State University, Moscow 119899, Russia

Received: March 17, 2006; In Final Form: May 4, 2006

The valence shell photoelectron spectrum, threshold photoelectron spectrum, and threshold photoelectron photoion coincidence (TPEPICO) mass spectra of acetone have been measured using synchrotron radiation. New vibrational progressions have been observed and assigned in the $\tilde{X}\ ^2B_2$ state photoelectron bands of acetone-h_6 and acetone-d_6, and the influence of resonant autoionization on the threshold electron yield has been investigated. The dissociation thresholds for fragment ions up to 31 eV have been measured and compared to previous values. In addition, kinetic modeling of the threshold region for $CH_3^\bullet$ and CH_4 loss leads to new values of 78 ± 2 kJ mol^{-1} and 75 ± 2 kJ mol^{-1}, respectively, for the 0 K activation energies for these two processes. The result for the methyl loss channel is in reasonable agreement with, but slightly lower than, that of 83 ± 1 kJ mol^{-1} derived in a recent TPEPICO study by Fogleman et al. The modeling accounts for both low-energy dissociation channels at two different ion residence times in the mass spectrometer. Moreover, the effects of the ro-vibrational population distribution, the electron transmission efficiency, and the monochromator band-pass are included. The present activation energies yield a $\Delta_f H_{298}$ for CH_3CO^+ of 655 ± 3 kJ mol^{-1}, which is 4 kJ mol^{-1} lower than that reported by Fogleman et al. The present $\Delta_f H_{298}$ for CH_3CO^+ can be combined with the $\Delta_f H_{298}$ for CH_2CO (−47.5 ± 1.6 kJ mol^{-1}) and H^+ (1530 kJ mol^{-1}) to yield a 298 K proton affinity for ketene of 828 ± 4 kJ mol^{-1}, in good agreement with the value (825 kJ mol^{-1}) calculated at the G2 level of theory. The measured activation energy for CH_4 loss leads to a $\Delta_f H_{298}$ ($CH_2CO^{+\bullet}$) of 873 ± 3 kJ mol^{-1}.

Introduction

The acetone ion ($C_3H_6O^{+\bullet}$) has been studied extensively over the last few decades and is the subject of a recent extensive review by McAdoo.[1] Perhaps the main interest in its chemistry has been that it is linked to its enol isomer by a 1,3-H shift that lies 145 kJ mol^{-1} above ionized acetone.[2] The ionized enol of acetone dissociates to $CH_3CO^+ + CH_3^\bullet$ by first isomerizing to ionized acetone. The reaction proceeds non-ergodically, favoring the departure of the newly formed methyl group.[1] Recent trajectory calculations starting at the 1,3-H shift barrier by Anand and Schlegel have also confirmed the nonergodic behavior.[2,3] As for ionized acetone itself, low internal energy ions lose only methane to form ionized ketene, $CH_2CO^{+\bullet}$. As the internal energy increases, methyl radical loss dominates.[1] Several attempts have been made to theoretically model the unimolecular chemistry of ionized acetone, and there is agreement on the qualitative aspects of the mechanism for the competing loss of methane and methyl radical (Scheme 1).[2,4−6] The energetics of the mechanism, however, are very sensitive to the theoretical treatment. The potential energy diagram for these two channels has been calculated most recently by Anand and Schlegel[2] at the CBS-APNO//QCISD/6-311G(d,p) and Wei et al.[6] at the G3 levels of theory (see also Heinrich et al.[4] and Ceño et al.[5] for calculations at the MP3 level of theory). The G3 and MP3 level calculations place the transition state for methane loss higher in energy than the products, which suggests that tunneling is important, but Schlegel's results indicate that this is not an issue. The experimental observation of an unusually large isotope effect ($k_H/k_D = 70$) associated with methane loss (CD_3H versus CH_3D) from the [1,1,1-d_3]acetone cation[7] supports the tunneling mechanism proposed by both Heinrich et al.[4] and Ceño et al.[5] Osterheld and Braumann,[8] however, performed infrared multiple photon dissociation experiments on the acetone and acetone-d_6 cations showing that tunneling does not occur and that the large apparent preference for abstraction of hydrogen arises from a competitive reaction isotope effect.

Photoelectron−photoion coincidence (PEPICO) spectroscopy is a useful experimental technique which allows the measurement of time-of-flight (TOF) mass spectra as a function of ion

10.1021/jp0616866 CCC: $33.50
Published on Web 06/21/2006

SCHEME 1: Mechanisms for the Competing Loss of Methane and the Methyl Radical from the Acetone Molecular Ion[a]

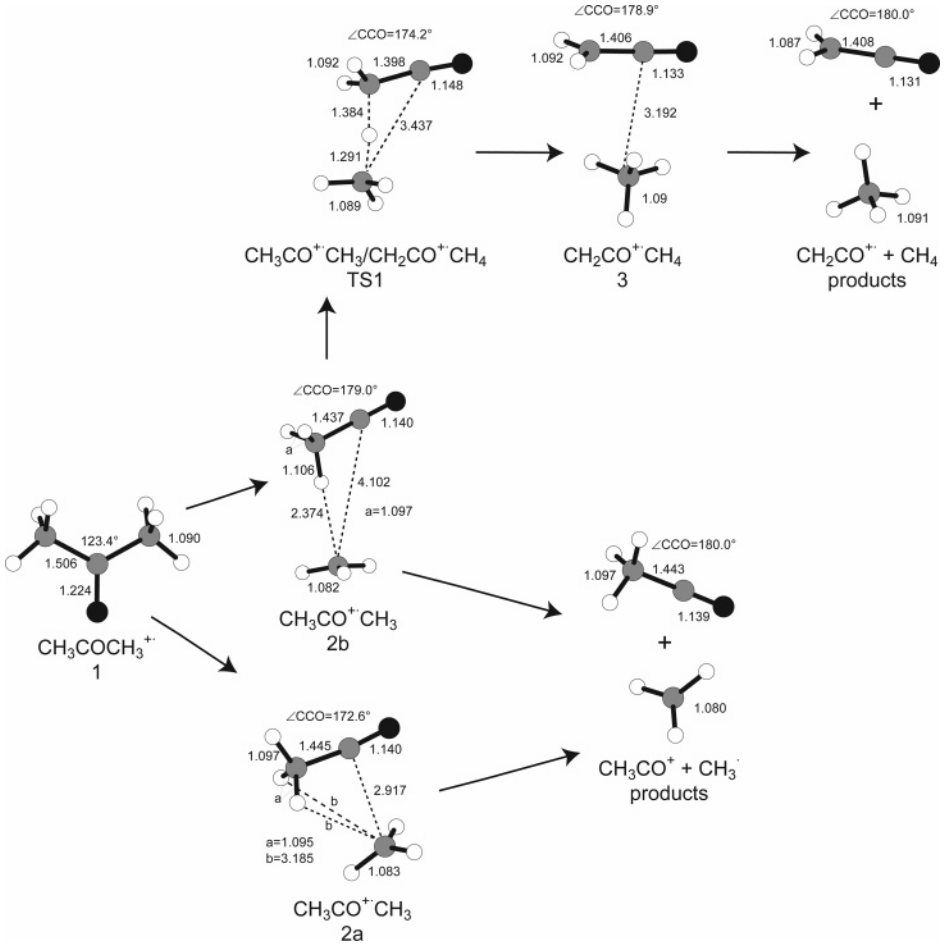

[a] MP2/6-31+G(d) geometries from this work have been used.

internal energy. From these spectra, dissociation rates and energetics can be extracted. However, with the exception of TPEPICO studies carried out by Stockbauer[9] and Fogleman et al.,[10] all previous coincidence investigations on acetone[11−15] were performed with energetic electrons, i.e., PEPICO experiments. As acetone has a large Franck−Condon gap in the region of the dissociation threshold, the measurement of TOF spectra close to the threshold, using the PEPICO technique, is extremely difficult. TPEPICO spectroscopy overcomes this limitation, because threshold (zero energy) electrons are produced through resonant autoionization even in energy ranges associated with Franck−Condon gaps. Hence, TPEPICO spectra may be measured in regions where the intensity of energetic electrons is practically zero.

We have recorded the threshold photoelectron spectrum and conventional energy analyzed photoelectron spectra of acetone, at photon energies of 40 and 80 eV, using synchrotron radiation. The observed bands have been assigned through comparison with vertical ionization energies and intensities computed using the outer valence Green function approach. The influence of resonant autoionization, particularly in the Franck−Condon gap between the $\tilde{X}\ ^2B_2$ and the $\tilde{A}\ ^2B_1$ state photoelectron bands, is discussed, together with the assignment of vibrational structure. In addition, TPEPICO mass spectra of acetone have been measured in the photon energy range 10.2−31 eV. These spectra have allowed dissociation thresholds for fragment ions to be derived, and the results are compared with previous values. Kinetic modeling of the threshold region for CH_4 and $CH_3^\bullet$ loss leads to new 0 K activation energies for these two processes and consequently to new heats of formation for the acetyl cation, CH_3CO^+, and ionized ketene, $CH_2CO^{+\bullet}$.

Experimental Details

The pulsed TPEPICO spectrometer,[16] in which the dissociation, kinetic, and threshold photoelectron studies on acetone were performed, and the 5 m normal incidence monochromator,[17] attached to the Daresbury Laboratory synchrotron radiation source, have been described in detail previously, so only a brief account will be given here. The diverging beam of radiation emerging from the monochromator exit slit was passed into a separately pumped vacuum chamber containing an ellipsoidal mirror. This mirror focused the radiation onto the entrance of a 1 mm i.d. glass capillary, which then transported the radiation into the spectrometer interaction region. With this arrangement, differential pumping was provided between the spectrometer and the monochromator. Lithium fluoride or indium filters, mounted in the differential pumping chamber, could be inserted into the beam to help suppress higher-order radiation. After passing through the interaction region, the incident radiation impinged upon a sodium salicylate coated screen, and the resulting fluorescence was detected with a photomultiplier. This signal could be used for normalization purposes. Photoionization occurred at the center of the interaction region where the radiation intersected a vertically directed beam of the gas being studied. The coincidence spectrometer employs a pulsed extraction technique,[9] the principal advantage of which is that threshold electrons can be detected with a high-energy resolu-

tion, while also allowing the associated ions to be collected with a high mass resolution. In the present arrangement,[16] a very low electric field is applied initially across the interaction region to extract threshold electrons. The detection system for the electrons consists of a lens specially designed for high transmission of low-energy electrons followed by a 100 mm mean radius hemispherical electrostatic analyzer. The lens accelerates the electrons to the chosen (typically 10 eV) analyzer pass energy, and the chromatic aberrations are such that only electrons having initially zero energy are brought to a focus at the analyzer entrance aperture. The detection of the electron triggers the application of a high-voltage (~1 kV) pulse across the interaction region to draw the ion toward the drift tube and initiates the TOF measurement. The time between the arrival of the electron and the arrival of the associated ion is measured electronically, with the summation of many events producing a TOF spectrum. Accumulation times varied from about 30 min to several hours. One of the advantages of the pulsed extraction technique is that breakdown curves can be measured as a function of ion residence time in the interaction region by varying the delay between the detection of the threshold electron and the application of the ion drawout field. The residence time is defined as the period between the creation of the electron−ion pair and the application of the pulse, and is given by the transit time of the electron added to the electronic signal processing time. With the present apparatus, the minimum residence time has been measured as 1116 ± 50 ns, using the experimental procedure described in Holland et al.[16] The breakdown curves for acetone in the threshold energy region were measured for two residence times by adding an additional electronic delay of 2 μs; that is, the actual residence times were 1.116 and 3.116 μs. The monochromator resolution was set at 0.04 nm (fwhm) (~4 meV in the relevant energy range). The electron transmission function, which is used in the convolution of the calculated breakdown curves, was derived from a threshold electron spectrum obtained from the photoionization of krypton in the region of the $^2P_{1/2}$ ionization limit under the conditions used in the TPEPICO measurements.

A threshold photoelectron spectrum of acetone-h_6 was recorded in the binding energy range 9−30 eV using only the electron detection part of the coincidence spectrometer. A similar spectrum of acetone-d_6 was obtained in the region of the $\tilde{X}\ ^2B_2$ state. The spectra were normalized to variations in the incident photon intensity using the signal from the photomultiplier. The monochromator resolution was set at 0.1 nm (fwhm) (~18 meV at $h\nu = 15$ eV). The binding energy scale for acetone-h_6 was calibrated using the values determined by Keane et al.[18] For acetone-d_6, a spectrum of the sample mixed with krypton was recorded. Since the ionization energies of krypton are well-known, this procedure enabled the binding energy scale of acetone-d_6 to be calibrated.

In a separate experiment, valence shell photoelectron spectra of acetone were recorded at photon energies of 40 and 80 eV over the same binding energy region (9−30 eV). The spectra were recorded with a hemispherical electrostatic electron energy analyzer[19] which was set at the so-called magic angle such that the measured intensity is independent of the asymmetry parameter. The raw data have been corrected for the kinetic energy dependent transmission function of the analyzer,[19] and the binding energies reported by Keane et al.[18] were used for calibration.

The metastable ion (MIKES) mass spectra[20] were obtained in the second field free region of a modified VG ZAB mass spectrometer[21] incorporating a magnetic sector followed by two electrostatic sectors (BEE geometry).

TABLE 1: G3 Total Energies[a] (in hartrees) for All Species in This Study

	E_0 (G3)	ZPE
$(CH_3)_2CO$ (ketone)	−192.9966743	0.085419
CH_2COHCH_3 (enol)	−192.9789675	0.085480
$C_2H_5^\bullet$	−79.06284058	0.061171
$HCO^\bullet$	−113.7916787	0.013397
CH_4	−40.45681706	0.046047
$CH_3^\bullet$	−39.79362574	0.030583
$^3CH_2$	−39.11771745	0.017939
$H^\bullet$	−0.5010029	
$(CH_3)_2CO^{+\bullet}$ (ketone) **1**	−192.6390334	0.083816
$CH_2COHCH_3^{+\bullet}$ (enol)	−192.6527362	0.085017
$CH_3COCH_2^+$	−192.0381107	0.074183
CH_3CO^+	−152.8180942	0.045279
CH_2COH^+	−152.7523916	0.043352
$CH_2CO^{+\bullet}$	−152.1535983	0.032787
HCO^+	−113.4912078	0.013215
$C_2H_5^+$	−78.76274643	0.062769
$CH_3CO^{+\bullet}CH_3$ (a) **2a**	−192.6173772	0.078530
$CH_3CO^{+\bullet}CH_3$ (b) **2b**	−192.6160249	0.077897
$CH_2CO^{+\bullet}CH_4$ **3**	−192.6152967	0.079734
H shift (TS)[b] **TS1**	−192.6085895	0.075719
keto−enol 1,3 H shift (TS)	−192.5808706	0.079726

[a] Based on optimized MP2/6-31+G(d) geometries and vibrational frequencies. [b] An optimized geometry for this TS was only obtained by keeping C1−H and H−C3 bond distances constant at values of 1.384 and 1.291 Å, respectively. These values were taken from the MP3/6-311G(d,p) calculations of Ceño et al.[5]

TABLE 2: Comparison of G3 and Experimental Relative Energies for the Acetone Ion and Its Fragmentation Products

	relative E_0 (G3 0 K) (kJ mol^{-1})	experimental relative enthalpies (kJ mol^{-1})
$(CH_3)_2CO$ (ketone)	−939	−936[26,27]
CH_2COHCH_3 (enol)	−892	−893,[26] −895[27]
$(CH_3)_2CO^{+\bullet}$ (ketone)	0	0
$CH_2COHCH_3^{+\bullet}$ (enol)	−36	−56,[26] −58[27]
$CH_3COCH_2^+ + H^\bullet$	262	
$CH_3CO^+ + CH_3^\bullet$	72	91,[26] 80[27]
$CH_2COH^+ + CH_3^\bullet$	244	230[26]
$CH_2CO^{+\bullet} + CH_4$	75	87,[26] 86[27]
$HCO^+ + C_2H_5^\bullet$	223	226,[26] 224[27]
$HCO^+ + CH_3^\bullet + CH_2$	621	639,[26] 642[27]
$C_2H_5^+ + HCO^\bullet$	222	228[26, 27]
$CH_3CO^{+\bullet}CH_3$ (a)	57	
$CH_3CO^{+\bullet}CH_3$ (b)	60	
$CH_2CO^{+\bullet}CH_4$	62	
H shift (TS)	80	
keto−enol 1,3 H shift (TS)	153	

Computational Procedures

Standard ab initio molecular orbital calculations[22] were performed using the *Gaussian 98*[23] suite of programs. Geometries for the ionic and neutral species were optimized and harmonic vibrational frequencies were calculated at the MP2/6-31+G(d) level of theory. The resulting MP2/6-31+G(d) geometries and zero-point energies (ZPEs) (scaled by 0.967)[24] were then used to obtain G3[25] total energies. These energies are listed in Table 1. The relative energies, given in relation to the acetone molecular ion, are summarized in Table 2, along with the relevant dissociation energies. In our thermochemical estimations, the recommended heats of formation tabulated in the NIST Chemistry Database[26] and by Lias et al.[27] have been used unless stated otherwise.

TABLE 3: Calculated (G3) and Experimental Enthalpies of Formation for All Optimized Species in This Study

	$\Delta_f H_0$(G3) (kJ mol^{-1})	$\Delta_f H_{298}$(G3) (kJ mol^{-1})	exptl $\Delta_f H_0$[10] (kJ mol^{-1})	exptl $\Delta_f H_{298}$ (kJ mol^{-1})
$(CH_3)_2CO$ (ketone)	−200	−216	−202.2 ± 0.6	−218.5 ± 0.6,[26] −217.2[27]
CH_2COHCH_3 (enol)	−153	−170		−176[26, 27]
C_2H_5•	133	123		119 ± 2,[26] 118[27]
HCO•	40	40		42 ± 4,[26] 44.8[27]
CH_4	−66	−74	−66.4 ± 0.4	−74.5 ± 0.4[26, 27]
CH_3•	144	141	150.3 ± 0.4	147.1 ± 1,[10, 26] 145.8[27]
$^3CH_2$	387	388		386,[26] 390[27]
H•	216	216	216	218[26, 27]
$(CH_3)_2CO^{+}$• (ketone)	739	724	734.5 ± 0.7	718.2 ± 0.6,[26 a] 719.2,[27] 718.8 ± 0.7[10]
$CH_2COHCH_3^{+}$• (enol)	703	687		661[26, 27]
$CH_3C(O)CH_2^{+}$	785	772		
CH_3CO^{+}	667	660	662 ± 3[c]	661,[26] 653,[27] 659.4 ± 1.1,[10] 655.5 ± 0.8,[30] 655 ± 3[c]
CH_2COH^{+}	839	833		803[27]
CH_2CO^{+}•	880	877	876 ± 3[c]	879,[26] 879.6,[27] 874.4 ± 1,[30] 873 ± 3[c]
HCO^{+}	829	829		824 ± 8,[26] 825.6[27]
$C_2H_5^{+}$	921	909		902 ± 2,[26 b] 902[27]
CH_3CO^{+}•CH_3 (a)	796	786		
CH_3CO^{+}•CH_3 (b)	799	790		
CH_2CO^{+}•CH_4	801	793		

[a] Estimated using the heat of formation of the neutral molecule of −218.5 kJ mol^{-1} [26] and the experimental ionization energy (9.708 eV).[18] [b] Estimated using the heat of formation of the neutral molecule and the experimental ionization energy (8.117 ± 0.008).[26] [c] Present work.

G3 theory approximates the energy of a species at the QCISD-(T)/G3large level of theory by a series of additive corrections to a base MP4/6-31G(d) energy. The G3large basis set is a modified version of the standard 6-311+G(3df,2p) basis set in which more polarization functions are added to first-row elements (3d2f), fewer on second-row elements (2df), and core polarization functions are incorporated. Details of the properties of the G3large basis set can be found in the original publication by Curtis et al.[25] G3 normally incorporates a scaled (by 0.8929) HF/6-31G(d) zero-point vibrational energy, spin−orbit corrections for atoms, and the use of the MP2(full)/G3large calculation to take into account core correlation contributions. Finally, an empirical higher-level correction accounts for residual basis set errors. In this work, we have replaced the MP2(full)/6-31+G-(d) equilibrium geometry and the HF/6-31G(d) ZPE with a MP2/6-31+G(d) geometry and ZPE scaled (by 0.9434) in the G3 calculation. The effect of substituting improved geometries and the corresponding ZPEs has been investigated for the N_2 neutral and ion using HF, MP2, B3LYP, and QCISD theories with a 6-31G(d) basis set.[28] The effect produced was negligible when compared to the errors inherent in the G3 calculations.

The G3 total energies were translated to enthalpies of formation according to the atomization procedure described by Nicolaides et al.[29] Thermal corrections to 298 K employed the scaled MP2/6-31+G(d) frequencies and known thermal corrections for the elements. Table 3 compares these results with experimental values.

Optimized MP2/6-31+G(d) C_1 and C_{2v} structures for ground-state acetone have been used to compute the vertical ionization energies and photoelectron spectral intensities or pole strengths, denoted P, using the outer valence Green function (OVGF)[31] with the frozen core orbital approximation and CC-pVTZ basis set (ROVGF(FC)/CC-pVTZ). The C_{2v} optimized structure has one low negative frequency of −35 cm^{-1} (∼4 meV) corresponding to rotation of the methyl groups. At room temperature, the methyl groups may be considered as free rotors, and the symmetry may be assumed to be C_{2v}. A comparison of the ionization energies and pole strengths of the two structures shows that the differences are negligible.

The two lowest-energy dissociation channels were modeled with the standard RRKM rate expression

$$k(E) = \frac{\sigma}{h}\frac{N^{\ddagger}(E - E_0)}{\rho(E)} \quad (1)$$

where $k(E)$ is the unimolecular rate constant at an ion internal energy, E, σ is the reaction degeneracy or symmetry number, h is Planck's constant, E_0 is the activation energy, $\rho(E)$ is the reactant ion density of states, and $N^{\ddagger}(E - E_0)$ is the transition-state sum of states.[32,33] The density and sum of states calculations employed the direct count algorithm of Beyer and Swinehart.[34] It is necessary to know, or to guess, the barrier height or activation energy and the vibrational frequencies of both the reactant ion and the transition state. The acetone ion frequencies were taken from the MP2/6-31+G(d) geometry. The transition state frequencies were obtained by removing one mode due to the reaction coordinate and scaling the remaining acetone ion frequencies until a satisfactory RRKM fit was obtained. The RRKM method allows the microcanonical rate constant, for a range of particular internal energies, to be calculated for each dissociation channel. These rate constants can then be used to calculate the theoretical breakdown curve at a chosen ion residence time.

The next step in the analysis procedure involves convoluting the theoretical curves with various experimental factors. These factors take into account the following: (1) the parent ion thermal (rotational and vibrational) energy, (2) the monochromator band-pass (photon resolution), and (3) the threshold electron analyzer transmission efficiency. The thermal population of the neutral molecule, $P(E', T)$, is given by

$$P(E', T) = \frac{P(E')\, e^{-E/k_B T}}{Q(T)} \quad (2)$$

where E' is the internal energy of the neutral molecule, k_B is the Boltzmann constant, T is the temperature, and $Q(T)$ is the vibrational or rovibrational function. $P(E', T)$ was calculated using solely a vibrational population and using a full ro-vibrational population. As the difference in E_0, obtained with these two populations, was non-negligible, the ro-vibrational densities and sums of states were used in the RRKM calculations. The effect of ab initio theory level and basis set was found to be negligible as long as the resulting frequencies were scaled. Figure 1 shows the thermal population for vibrational and

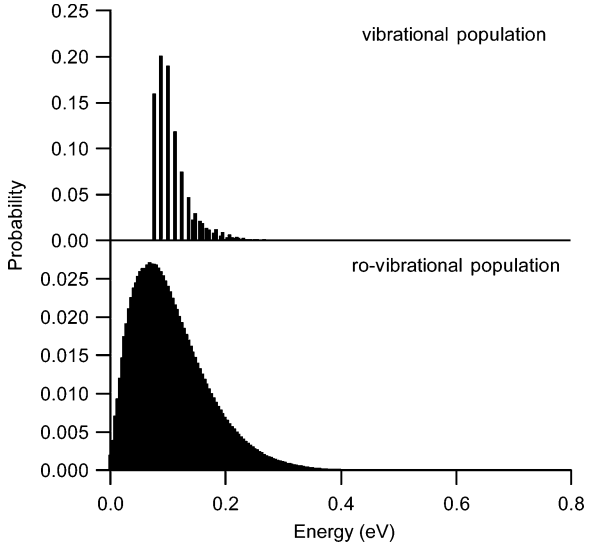

Figure 1. Upper frame: the vibrational populations of neutral acetone at a temperature of 298 K. Lower frame: the ro-vibrational population thermal distribution for molecular acetone, at a temperature of 298 K.

ro-vibrational levels. The convolution of the internal energy distribution with the theoretical breakdown curve produces a very significant effect near threshold.

The photon resolution was set at ~4 meV in the relevant energy range, and the convolution of the Gaussian function representing this band-pass had little effect on the breakdown curves. Finally, the theoretical curves were convoluted with the threshold electron analyzer transmission efficiency with a width of ~9 meV (fwhm).

In summary, theoretical breakdown curves were produced from the unimolecular rate constants, $k(CH_3CO^+)$ and $k(CH_2\text{-}CO^{+\bullet})$, and were then convoluted with relevant experimental parameters. The activation energy, E_0, and the transition states frequencies were varied until a satisfactory fit to the experimental breakdown curves, obtained at ion residence times of 1.116 and 3.116 μs, was found.

Results and Discussion

Photoelectron Spectra. The valence shell photoelectron spectrum of acetone-h_6 has been recorded previously using HeI[35−38] and HeII[18,39,40] radiation, and the threshold photoelectron spectrum has been measured in the vicinity of the $\tilde{X}\ ^2B_2$ state using continuum sources.[9,41] Most of the observed features have been assigned, based upon the results from molecular orbital calculations, although there remains some uncertainty regarding the ordering of the ionic states occurring in the binding energy range 15−17 eV.[18,40,42,43] In the present work, the valence shell photoelectron spectrum of acetone has been measured in the binding energy range 9−30 eV using monochromatic synchrotron radiation with an energy of 80 eV. In addition, the threshold photoelectron spectrum has been recorded in the same binding energy range. A comparison between these two spectra allows the influence of resonant autoionization on the threshold photoelectron yield to be assessed.

By combining the results from the present OVGF calculations (Table 4) with those of Bieri et al.[40] for the inner valence orbitals, the ground state electronic configuration of acetone (using C_{2v} symmetry) may be written as in Chart 1.

CHART 1

$$(\text{core})^8\underbrace{(4a_1)^2\,(5a_1)^2\,(2b_2)^2}_{\text{inner valence}}\underbrace{(6a_1)^2\,(1b_1)^2\,(7a_1)^2\,(3b_2)^2\,(1a_2)^2\,(8a_1)^2\,(4b_2)^2\,(2b_1)^2\,(5b_2)^2}_{\text{outer valence}}$$

TABLE 4: Calculated Energies (*E*) and Intensities (*P*) for Valence Orbital Vertical Ionization in Acetone Using ROVGF(FC)/CC-pVTZ Level of Theory

MO number	MO	exptl IE_v (eV)	character[a]	C_{2v} geometry OVGF *E* (eV)	*P*	MO	C_1 geometry OVGF *E* (eV)	*P*
16	$5b_2$	9.708,[18] 9.70[37]	n_0, (π_{CH3}^-)	9.96	0.90	16a	9.96	0.90
15	$2b_1$	12.4,[18] 12.59[37]	$\pi_{C=O}$	12.55	0.89	15a	12.55	0.89
14	$4b_2$	13.4,[18] 13.41[37]	π_{CH3}^- (σ_{CO})	13.60	0.91	14a	13.60	0.91
13	$8a_1$	14.0,[18] 14.04[37]	σ_{CO}, σ_{CC}^+	14.16	0.91	13a	14.16	0.91
12	$1a_2$	14.5,[18] (14.8)[37]	π_{CH3}^-	14.36	0.92	12a	14.37	0.92
11	$1b_1$	16.4,[18] 15.60[37]	π_{CH3}^+ (π_{CO})	15.96	0.91	11a	15.96	0.91
10	$7a_1$	15.6,[18] (16.1)[37]	σ_{CO}	15.77	0.90	10a	15.77	0.90
9	$3b_2$	15.9,[18] (16.6)[37]	σ_{CC}^- (σ_{CO})	15.73	0.89	9a	15.73	0.89
8	$6a_1$	17.813[18]	C_1 2s	18.27	0.89	8a	18.27	0.89

[a] The main characters for each molecular orbital have been expressed as the following: Bonding between p_y and p_z orbitals, i.e., in-plane bonding, has been designated as σ bonding. Similarly, out-of-plane bonding, p_x orbitals, has been designated as π. The $\pm$ signs are based on the symmetry elements of the point group of the molecule; in the acetone case (C_{2v}), they also indicate positive/negative overlap between two symmetrically identical bonds or substituents, e.g., the σ_{CC}^+ notation means that there is positive σ_{CC} bonding between both CC bonds in acetone, and in addition, the overlap CCC is also positive (a negative sign in this instance would mean that, while both CC bonds have a positive overlap, a node exists on the central C, and the net CCC overlap is negative). The symbol π_{CH3} indicates the pseudo π orbitals of the CH_3 group.

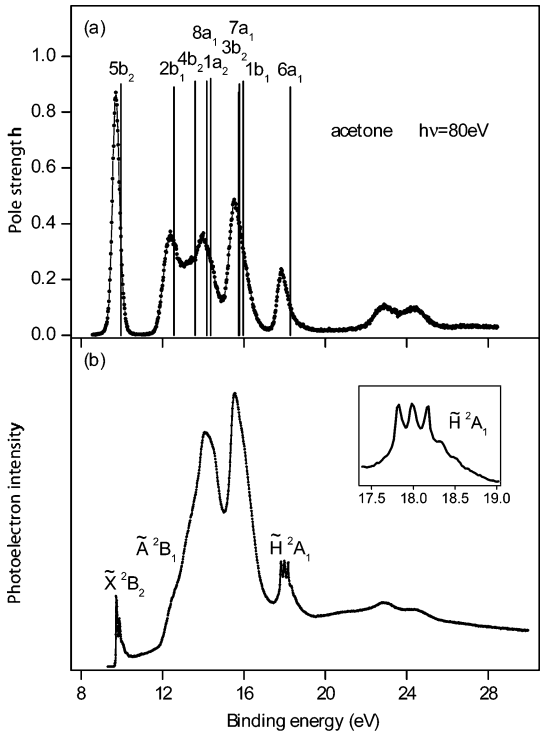

Figure 2. (a) The valence shell photoelectron spectrum of acetone recorded at a photon energy of 80 eV. (b) The valence shell threshold photoelectron spectrum of acetone.

The photoelectron spectrum of acetone recorded at 80 eV is plotted in Figure 2a, together with the present OVGF calculations. The intensity of the bars is proportional to the calculated pole strength. A spectrum (not shown) was also recorded at a photon energy of 40 eV and was almost identical to that plotted in Figure 2a. This similarity suggests that the spectrum shown in Figure 2a results, essentially, from direct photoionization and is not significantly influenced by autoionization. The photoelectron spectrum obtained using an excitation energy of 80 eV displays the same features observed in those recorded using

HeI or HeII radiation, apart from some minor intensity differences attributable to small variations in the energy-dependent photoionization partial cross sections. With the higher resolution attainable using HeI or HeII radiation, short vibrational progressions have been observed in the $(5b_2)^{-1}\tilde{X}\ ^2B_2$ and the $(6a_1)^{-1}\tilde{H}\ ^2A_1$ state bands.[18,35−38]

The extended 2ph-TDA calculations[32] demonstrate that the molecular orbital model of ionization[44] holds for orbitals with binding energies up to ∼18 eV but does not apply to the inner valence $4a_1$, $5a_1$, and $2b_2$ orbitals. Bieri et al.[40] predict that ionization from the $2b_2$ and $5a_1$ orbitals gives rise to several satellite states clustered around binding energies of ∼24 and 26 eV, respectively. The two corresponding experimental features are discernible around 23 and 24.5 eV (Figure 2a). An additional very weak and broad peak, associated with ionization from the $4a_1$ orbital, has been observed by Potts et al.[39] at a binding energy of 34 eV. According to Bieri et al., the intensity originating from the $4a_1$ orbital is distributed over numerous low intensity satellites covering the 30−40 eV region.

The effect of resonant autoionization on the threshold photoelectron yield is evident through a comparison of the spectra shown in Figure 2a,b. Direct ionization results in the $\tilde{X}\ ^2B_2$ state photoelectron band being the most intense. In contrast, the two strongest features in the threshold photoelectron spectrum (Figure 2b) have maxima at 14.2 and 15.6 eV. It is also noticeable that the threshold photoelectron yield remains finite across the entire excitation range. This is particularly evident in the Franck−Condon gap (∼10.5−11.8 eV) between the bands due to the $\tilde{X}\ ^2B_2$ and $\tilde{A}\ ^2B_1$ states. It is, of course, this threshold photoelectron production by resonant autoionization which allows breakdown curves to be measured in Franck−Condon gap regions using TPEPICO techniques.

Keane et al.[18] determined vertical binding energies of 12.4, 13.4, 14.0, and 14.5 eV for the photoelectron bands associated with the $2b_1$, $4b_2$, $8a_1$, and $1a_2$ orbitals, respectively. In this binding energy range, the threshold photoelectron spectrum is dominated by a peak with a maximum at 14.2 eV. However, additional features, due to ionization from the $2b_1$ and $4b_2$ orbitals, are discernible at 12.3 and 13.2 eV as gradient changes on the rising edge. A shoulder, at ∼14.5 eV, probably correlates with a similar weak feature, attributed to the $1a_2$ orbital, in the HeII excited spectrum.[18] The present results demonstrate that autoionization from Rydberg series converging onto ionization limits occurring between ∼12 and 17 eV strongly affects threshold photoelectron production in the outer valence region. Excited valence states may also play a role. Unfortunately, however, although detailed theoretical studies[45] have been made on the Rydberg series converging onto the $\tilde{X}\ ^2B_2$ limit, and on the low-lying valence states, much less information is available concerning the energy region lying above the ionization threshold.

The most intense feature in the threshold photoelectron spectrum has a maximum at 15.6 eV and can be associated with ionization from the $1b_1$, $7a_1$, and $3b_2$ orbitals. Again, the prominence of this feature can be attributed to resonant autoionization.

The last orbital for which the single particle model applies is $6a_1$, and ionization from this orbital gives rise to the photoelectron band ($\tilde{H}\ ^2A_1$) at a binding energy of ∼18 eV. In the threshold photoelectron spectrum, this band exhibits a prominent vibrational progression with a spacing of ∼168 meV (Table 5). At higher energies, three very broad features are discernible at 20.8, 22.9, and 24.5 eV. The latter two features have counterparts in the photoelectron spectrum recorded at 80 eV (Figure 2a) and are due to the groups of satellites predicted for the inner valence $2b_2$ and $5a_1$ orbitals.[40] The first of the features, at 20.8 eV, might be associated with higher-order configuration interaction states not included in the calculations of Bieri et al.

TABLE 5: The Binding Energies and Possible Assignments of Vibrational Structure Observed in the $\tilde{X}\ ^2B_2$ and the $\tilde{H}\ ^2A_1$ State Threshold Photoelectron Bands of Acetone

$\tilde{X}\ ^2B_2$ state			$\tilde{H}\ ^2A_1$ state	
	binding energy (eV)			
assignment	acetone-h_6	acetone-d_6	assignment	binding energy (eV)
8_1^0	9.661	9.672	0_0^0	17.821
0_0^0	9.708	9.714	4_0^1	17.988
8_0^1	9.749	9.746	4_0^2	18.162
8_0^2	9.788		4_0^3	18.330
6_0^1	9.837	9.816	4_0^4	18.497
5_0^1	9.866	9.835		
$6_0^1 8_0^1$	9.873			
$5_0^1 8_0^1$	9.904	9.867		
$6_0^1 8_0^2$	9.915			
$5_0^1 6_0^1$	9.994	9.934		
$5_0^1 6_0^1 8_0^1$	10.031			
$5_0^1 6_0^1 8_0^2$	10.070			
unidentified		10.10		
unidentified	10.24	10.22		

Figure 3a,b shows the vibrational structure discernible in the $\tilde{X}\ ^2B_2$ state threshold photoelectron bands of acetone-h_6 and acetone-d_6, respectively, and possible assignments are given in Table 5. Some of this structure in acetone-h_6 has been observed previously.[18,35−38,41] However, the improved quality of the present data allows more features to be identified, and this has led to a partial reanalysis of earlier assignments. The excitation of various totally symmetric vibrational modes in the $\tilde{X}\ ^2B_2$ state photoelectron band of normal and deuterated acetone has also

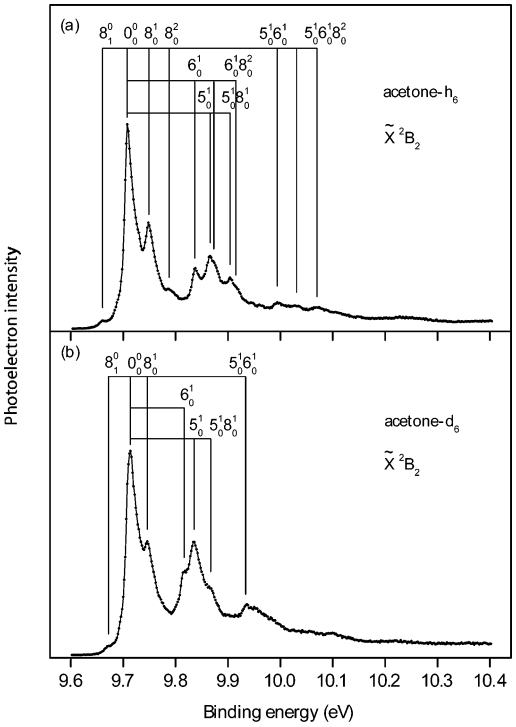

Figure 3. (a,b) show the $\tilde{X}\ ^2B_2$ state threshold photoelectron bands of acetone-h_6 and acetone-d_6, respectively. The binding energies and possible assignments of vibrational structure are given in Table 5.

been studied by ter Steege et al.[46] using multiphoton ionization. Their work enabled the following energies to be determined: ν_3^+ (CO stretch) 191 meV, ν_4^+ (CH_3-d-deform) 175 meV, ν_6^+ (CH_3 rock) 130 meV, ν_7^+ (CC stretch) 85 meV, and ν_8^+ (CCC deform) 42 meV, in acetone-h_6, and ν_4^+ 128 meV, ν_5^+ 120 meV, ν_6^+ 99 meV, and ν_8^+ 29 meV, in acetone-d_6.

The outermost $5b_2$ molecular orbital is non-bonding and approximates to a lone-pair localized on the oxygen atom. Consequently, the HeI excited $\tilde{X}\ ^2B_2$ state photoelectron band displays little vibrational structure. In contrast, the progressions observed in the corresponding threshold photoelectron band are more extensive, and this enhancement can be attributed to resonant autoionization. All previous studies of the ground state photoelectron band of acetone-h_6 have consistently assigned some of the vibrational structure to excitation of the ν_8^+ mode. However, the identification of other vibrational features is less firmly established.

The progressions observed in the present $\tilde{X}\ ^2B_2$ state threshold photoelectron band of acetone-h_6 can be ascribed to excitation involving one or more of the ν_5^+, ν_6^+, or ν_8^+ vibrational modes, where ν_5 (CH_3-s-deform) has an energy of 169 meV in the $\tilde{X}\ ^1A_1$ state of the neutral.[46] Excitation of the ν_8^+ mode, with one or two quanta, gives rise to the peaks at 9.749 and 9.788 eV, respectively. These two peaks correlate with steps observed in the photoion yield curve measured by Trott et al.[47] In the binding energy range 9.83−9.95 eV, three peaks are discernible. The first of these peaks, located at 9.837 eV, is ascribed to single excitation of the ν_6^+ mode, in agreement with the assignment proposed by Furuya et al.[41] However, the present data suggest that the two peaks at higher binding energies, 9.87 and 9.9 eV, are each due to more than a single vibrational excitation. The peak at 9.87 eV is broad and shows indications of two components located at 9.866 and 9.873 eV. These energies fit well with 5_0^1 and $6_0^1 8_0^1$ excitations, respectively. Such an assignment implies a reduction by ~7% in the energy of the ν_5 mode from its value in the neutral ground state, which seems reasonable. The peak around 9.9 eV has been assigned by Furuya et al. to the 3_0^1 excitation.[41] However, a doublet structure may be inferred for this feature with components located at 9.904 and 9.915 eV. These components fit well with the assignments already proposed for the doublet structure at 9.87 eV, with a simple addition of a quantum of the ν_8^+ mode. By such assignments, a consistent picture of the vibrational excitations is obtained involving modes localized in the CH_3-C-CH_3 complex. This is consistent with the character of the $5b_2$ orbital in the OVGF calculations.

At higher binding energy, a sequence of three previously unobserved peaks, with a spacing of ~38 meV, can be assigned to the $5_0^1 6_0^1$, $5_0^1 6_0^1 8_0^1$, and $5_0^1 6_0^1 8_0^2$ excitations. A final broad peak, with no resolved structure, appears around 10.24 eV.

The vibrational progression in the $\tilde{X}\ ^2B_2$ state threshold photoelectron spectrum of acetone-d_6 (Figure 3b) can be assigned in a manner analogous to that used for acetone-h_6. The reduction in the vibrational energies for the deuterated molecule results in less structure being resolved. Nevertheless, the similarity in the vibrational progressions for acetone-h_6 and acetone-d_6 provides support for the proposed assignments (Table 5). The asymmetric feature occurring in the binding energy range ~9.9−10.0 eV in acetone-d_6 undoubtedly contains several vibrational components, as observed in acetone-h_6, but the individual contributions are not discernible due to strong overlap. Two broad but unidentified peaks are located at 10.10 and 10.22 eV, with the latter peak constituting the counterpart of the feature at 10.24 eV in acetone-h_6.

The vibrational structure discernible in the $\tilde{H}\ ^2A_1$ state band of acetone-h_6 at 18 eV can be understood in terms of a single progression in the ν_4^+ mode, the energy of which is 175 meV in the $\tilde{X}\ ^2B_2$ state band.[46] Because of a more complex bonding situation in the $\tilde{H}\ ^2A_1$ state compared to that in the $\tilde{X}\ ^2B_2$ state, the energy of the ν_4^+ mode in the $\tilde{H}\ ^2A_1$ state is expected to be somewhat lower than that in the $\tilde{X}\ ^2B_2$ state. The observed separation between the vibrational components is ~168 meV, which appears reasonable. However, the energy spacings are not entirely consistent, the line shapes are somewhat variable, and the relative intensities do not correspond to a normal Franck−Condon profile. Therefore, it appears that vibrational modes, other than that forming the dominant ν_4^+ progression, are being excited. It is also noticeable that the beginning of the band is superimposed upon a gradual rise and reaches a first maximum, corresponding to the adiabatic transition, at 17.821 eV. The features contributing to this gradual increase in intensity may be associated with hot-band transitions involving not only the low-energy, totally symmetric, ν_8 mode, but also vibrational modes of other symmetries. In particular, the ν_{12} (a_2) and ν_{24} (b_1) modes, with vibrational energies of 10 and 15 meV, respectively,[46] may be expected to be strongly excited in the room-temperature target molecules and could give substantial contributions through transitions involving no change in vibrational quantum numbers.

TPEPICO TOF Spectra and Resulting Breakdown Diagrams. Coincidence spectra were collected in the photon energy range 10.2−31 eV, and examples are shown in Figure 4. Only the acetone molecular ion was observed at energies below 10.3 eV. Appearance energies (AEs) of the fragment ions, derived from the TOF spectra, are listed in Table 6, along with literature values. In general, our AEs are in good agreement with previous values, although there are some notable discrepancies with results obtained in a recent photoionization (PI) study by Wei et al.[6] In most cases, our AEs are lower than their values, with the exception of those for *m*/*z* 39 and 41, for which our thresholds of 15.4 and 17.2 eV, respectively, are significantly higher. However, all these experimental results should be regarded as upper limits, since the thresholds may be affected by kinetic and competitive shifts. The TOF spectra (Figure 4) and the breakdown curves (Figures 5 and 6) indicate that the acetone parent ion is not observed at energies above 10.7 eV. This is contrary to the results obtained by Bombach et al.[15] where the detection of the parent ion at ~12 eV was attributed to formation from the $\tilde{A}\ ^2B_1$ state.

At energies below ~15 eV, the peak due to the CH_3CO^+ ion (*m*/*z* 43) completely dominates the TOF spectra with the only other significant feature arising from the $CH_2CO^{+\bullet}$ fragment ion (*m*/*z* 42) generated via methane loss, which occurs over a narrow energy range of 10.3−10.6 eV. Above 15 eV, peaks due to CH_3^+, $C_2H_3^+$, and $C_2H_2^{+\bullet}$ begin to emerge along with the reappearance of the $CH_2CO^{+\bullet}$ fragment. The $CH_2^{+\bullet}$ fragment also becomes prominent above 20 eV. In Table 7, a summary is given of the most pertinent fragmentation processes for the formation of a particular ion, together with the associated thermochemical thresholds. These thresholds have been evaluated using the heats of formation tabulated in the NIST database[26] as well as G3 thresholds calculated in this work. As this thermochemical estimation does not take into account the barriers in the reactions, the estimated thresholds will always have values lower than, or equal to, the AEs. It is not unusual for such barriers, for example, a hydrogen migration, to have energies as high as 1−2 eV. We can only estimate which fragmentation process produces the ion in question when that

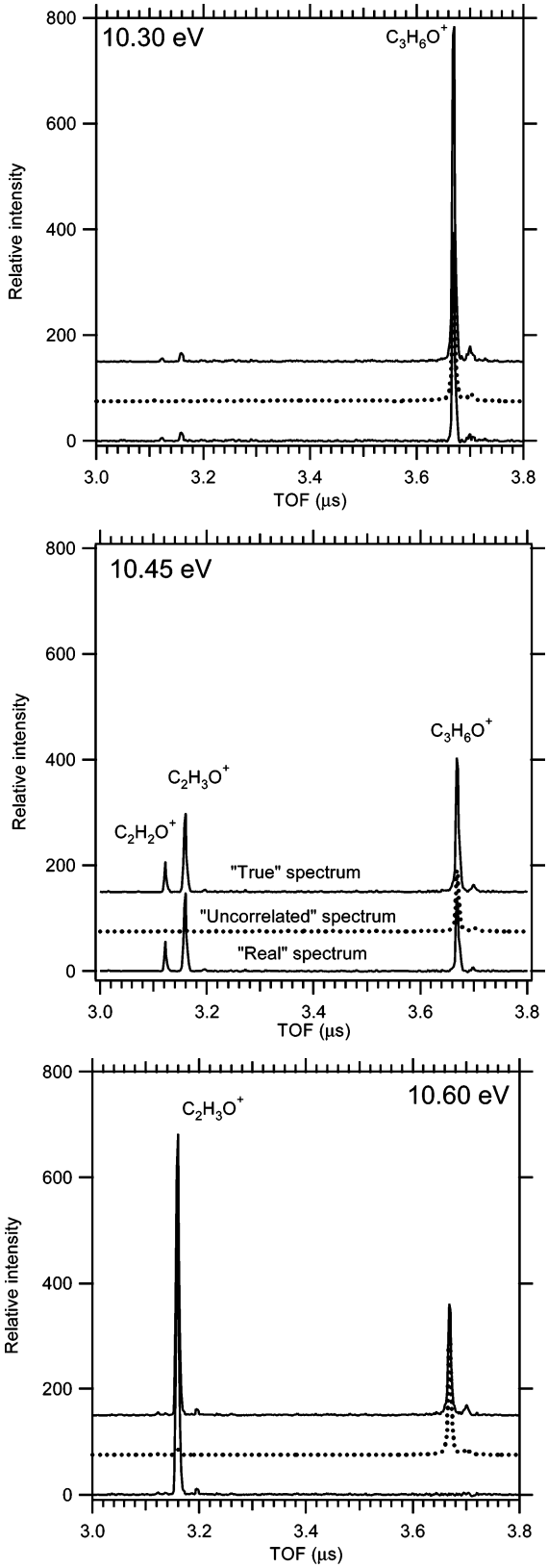

Figure 4. Typical TOF spectra showing the rapid change in ion channel intensity in the threshold region (shown at 10.30, 10.45, and 10.60 eV).

ion first appears. The reaction kinetics of the dissociation process are also important, and this effect will be apparent in cases where the most thermochemically favorable fragmentation is kinetically unfavorable. Under such circumstances, the observed AE will be higher than expected.

TABLE 6: Fragment Ion Appearance Energies

		experimental appearance energies at 298 K (eV)	
m/z	fragment ion	this work	literature[a]
43	$C_2H_3O^+$	10.30 ± 0.05	10.2,[52] 10.28,[53,54] 10.30,[55] 10.32,[10 b] 10.36(PI),[56] 10.37(PI),[57] 10.38(PI),[58] 10.42(PI),[59,60] 10.52(PI),[47] 11.3,[61] 12.22(PEPICO),[13] 10.49 ± 0.02 (PI)[6]
42	$C_2H_2O^{+\bullet}$	10.30 ± 0.05, 15[c]	10.7,[62] 10.32,[10,b] 10.53 ± 0.02 (PI)[6]
57	$C_3H_5O^+$	12.5 ± 0.2	13.1,[63] 13.10 ± 0.03 (PI)[6]
56	$C_3H_4O^{+\bullet}$	-	15.2,[62] 12.71 ± 0.03 (PI)[6]
29	HCO^+	13.4 ± 0.2	
15	CH_3^+	13.8	13.90(PEPICO),[64] 14.93,[65] 15.2,[61] 15.36,[66] 15.61(PEPICO),[13] 14.41 ± 0.03 (PI)[6]
28	$CO^{+\bullet}$ or $C_2H_4^{+\bullet}$	14.4	
26	$C_2H_2^{+\bullet}$	14.8	
27	$C_2H_3^+$	15.0	16.9,[67] 15.59 ± 0.04 (PI)[6]
31	CH_3O^+	15.0	
39	$C_3H_3^+$	15.4	14.51 ± 0.03 (PI)[6]
14	$CH_2^{+\bullet}$	16.6	
41	C_2HO^+ or $C_3H_5^+$	17.2	15.63 ± 0.04 (PI)[6]
40	$C_2O^{+\bullet}$ or $C_3H_4^{+\bullet}$	17.6	
13	CH^+	22	
38	$C_3H_2^{+\bullet}$	27	
25	C_2H^+	28	
37	C_3H^+	30	

[a] All AEs were derived from EI measurements unless stated otherwise. [b] From reported 298 K breakdown diagram. [c] Reappearance.

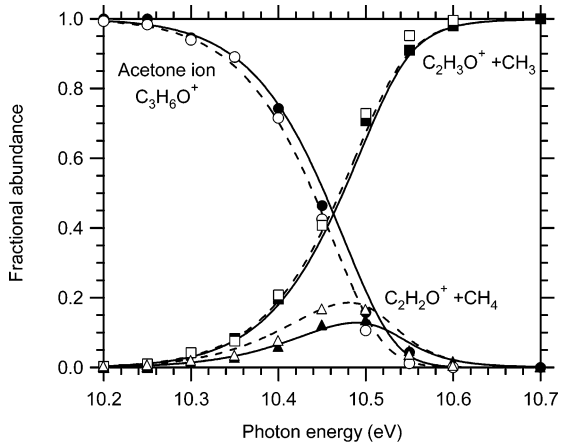

Figure 5. Threshold region breakdown diagram derived from the TOF spectra. The calculated curves are shown as solid lines (1.116 μs ion residence time) and dashed lines (3.116 μs ion residence time). The experimental data are as follows: (●, ○) $C_3H_6O^{+\bullet}$ (m/z = 58), (■, □) $C_2H_3O^+$ (m/z = 43), (▲, △) $C_2H_2O^{+\bullet}$ (m/z = 42); where the closed and open symbols represent ion residence times of 1.116 μs and 3.116 μs, respectively.

Methyl and Methane Loss. The threshold region for fragmentation of the acetone molecular ion occurs in the energy range 10.2−10.7 eV, and the corresponding breakdown diagram, derived from the TOF spectra, is shown in Figure 5. The observed low-energy dissociations produce the acetyl ion, CH_3CO^+ (m/z 43), and the ketene ion, $CH_2CO^{+\bullet}$ (m/z 42), associated with the loss of a methyl radical and methane, respectively. This energy region lies within the Franck−Condon gap between the photoelectron bands due to the $\tilde{X}\ ^2B_2$ and the $\tilde{A}\ ^2B_1$ states (Figure 2). Thus, the ions are formed by resonant autoionization, following the initial creation of a highly excited neutral state. This highlights the suitability of the TPEPICO technique to the study of molecular fragmentation and indicates the difficulties

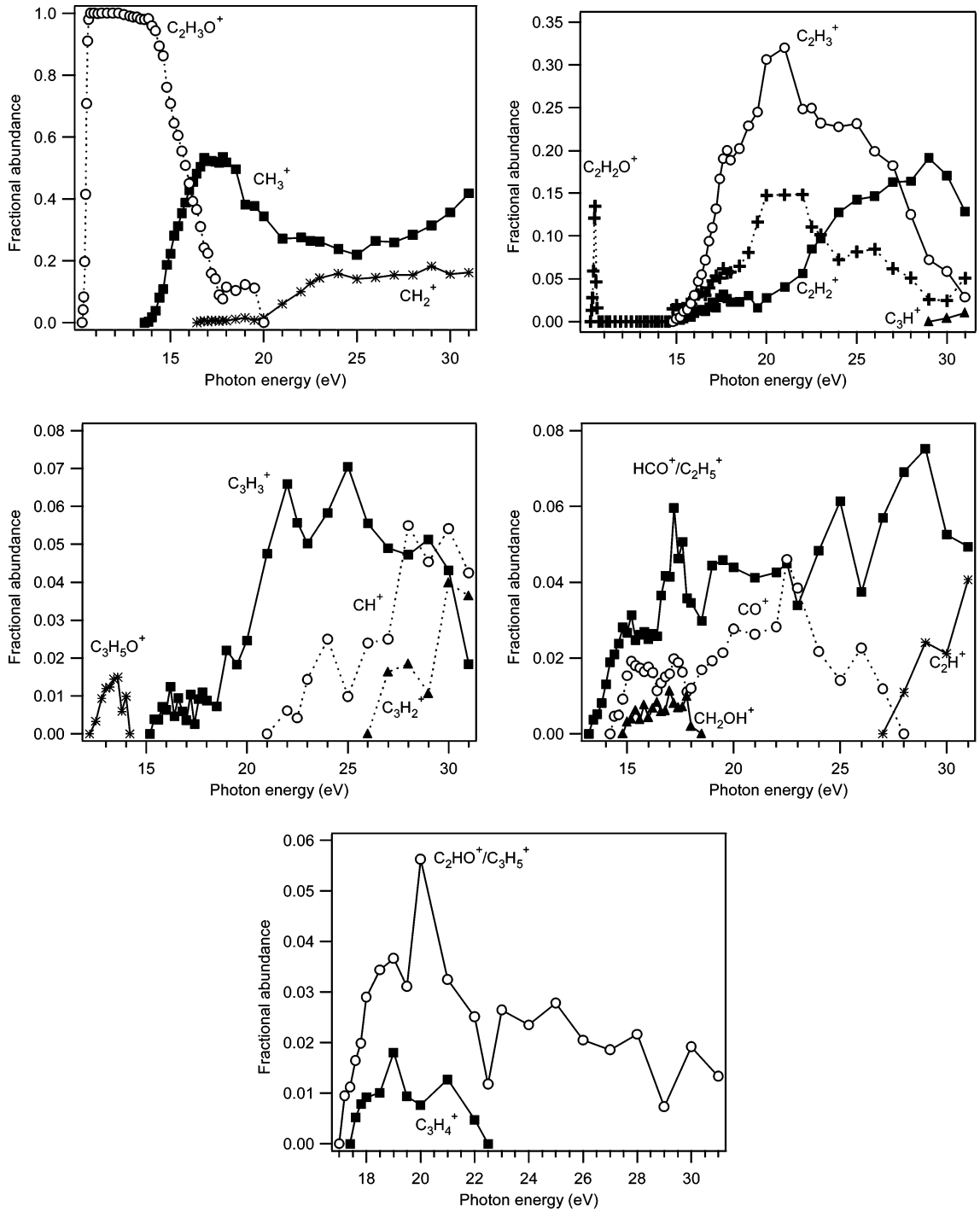

Figure 6. Breakdown diagrams up to 31 eV for all fragment ions.

encountered in investigations of the crossover region in acetone in previous PEPICO experiments.[11−15]

Recently, Fogleman et al.[10] measured the acetone breakdown diagram in detail in the threshold energy region between 10.2 and 10.8 eV using monochromatized vacuum ultraviolet radiation from a dispersed H_2 discharge lamp along with a TOF ion mass spectrometer and velocity-focusing optics for the electrons. The photon and electron energy resolutions employed in that study are similar to those used in the present investigation. Not surprisingly, therefore, the breakdown diagram obtained by Fogleman et al. is identical to that derived in the present study. According to our results, both the CH_3CO^+ and $CH_2CO^{+\bullet}$ ions appear at 10.30 ± 0.05 eV, in excellent agreement with the data of Fogleman et al.[10] as well as with earlier literature values (see Table 6).

The large uncertainty quoted with our AE is due solely to the energy spacing at which the TOF spectra were measured. Similar AEs for the CH_3CO^+ and $CH_2CO^{+\bullet}$ fragment ions have been reported in photoionization mass spectrometry studies.[6,48] McAdoo and Witiak[49] reported that the methyl loss channel is dominant for high internal energies of the reactant ion, whereas methane elimination is the major channel for low internal energies, i.e., metastable energies.

Figure 7 shows the MIKES spectrum of metastable acetone molecular ions obtained on the modified VG ZAB spectrometer at the University of Ottawa. Under conditions of low pressure

TABLE 7: Comparison of Experimental Appearance Energies with Thermochemical Thresholds Estimated from Literature $\Delta_f H$ Values as Well as Calculated G3 (298 K) Values Relative to Neutral Acetone

			estimated thermochemical thresholds at 298 K (kJ mol^{-1})	
m/z	fragment ion	AE (eV)	exptl[a]	G3
58	$CH_3C(O)CH_3^{+\bullet}$	9.708 ± 0.004[18]	9.7080 ± 0.0001,[68] 9.703 ± 0.006[26]	9.74
57	$CH_3C(O)CH_2^+ + H^\bullet$	12.5 ± 0.2		12.43
43	$CH_3CO^+ + CH_3^\bullet$	10.30 ± 0.05	10.64 ± 0.1, 10.53 ± 0.15,[27] 10.62 ± 0.01[10]	10.54
42	$CH_2CO^{+\bullet} + CH_4$	10.30 ± 0.05	10.6 ± 0.15	10.56
	$CH_2CO^{+\bullet} + CH_3^\bullet + H^\bullet$		15.2± 0.15	
41	$C_2HO^+ + CH_4 + H^\bullet$	17.2	15.4 ± 0.1	
	$C_3H_5^+ + OH^\bullet$		12.5 ± 0.15	
	$C_3H_5^+ + O + H^\bullet$		16.9 ± 0.1	
40	$C_3H_4^{+\bullet} + H_2O$	17.6	11.4 ± 0.1,[c] 12.1 ± 0.1,[d]	
	$C_3H_4^{+\bullet} + OH^\bullet + H^\bullet$		12.3 ± 0.1,[e] 16.6 ± 0.15,[c]	
			17.2 ± 0.15,[d] 17.5 ± 0.15[e]	
39	(cyclo-)$C_3H_3^+ + H_2O + H^\bullet$	15.4	(13.2 ± 0.1) 14.2 ± 0.1	
	(cyclo-)$C_3H_3^+ + OH^\bullet + H_2$		(13.9 ± 0.15) 14.9 ± 0.15	
38	(cyclo-)$C_3H_2^{+\bullet} + OH^\bullet + 3H^\bullet$	27	(21.6 ± 0.15) 21.9 ± 0.15[f]	
	(cyclo-)$C_3H_2^{+\bullet} + O^\bullet + 4H^\bullet$		(26.1 ± 0.1) 26.3 ± 0.1[f]	
37	C_3H^+	30		
31	$CH_2OH^+ + C_2H_3^\bullet$	15.0	12.81 ± 0.06	
	$CH_2OH^+ + C_2H_2 + H^\bullet$		14.32 ± 0.02	
	$CH_3O^+ + C_2H_3^\bullet$		16.3 ± 0.1	
29	$HCO^+ + C_2H_5^\bullet$	13.4 ± 0.2	12.04 ± 0.09	12.11
	$HCO^+ + CH_3^\bullet + CH_2$		16.3 ± 0.13	16.31
	$COH^+ + C_2H_5^\bullet$		13.5 ± 0.1[b]	
	$C_2H_5^+ + HCO^\bullet$		12.05 ± 0.05	12.07
28	$CO^{+\bullet} + C_2H_6$	14.4	14.3 ± 0.1	
	$CO^{+\bullet} + 2\,CH_3^\bullet$		18.2 ± 0.1	
	$C_2H_4^{+\bullet} + CH_2O$		12.2 ± 0.01	
27	$C_2H_3^+ + CH_2O + H^\bullet$	15.0	13.6 ± 0.1	
	$C_2H_3^+ + CH_3O^\bullet$		13.8 ± 0.1	
26	$C_2H_2^{+\bullet} + CO + 2H_2$	14.8	14.9 ± 0.1	
	$C_2H_2^{+\bullet} + CH_2O + H_2$		14.9 ± 0.1	
25	C_2H^+	28		
15	$CH_3^+ + CH_3CO^\bullet$	13.8	13.5 ± 0.1	
	$CH_3^+ + CH_3^\bullet + CO$		14.0 ± 0.1	
14	$CH_2^{+\bullet}$	16.6		
13	CH^+	22		

[a] All $\Delta_f H$ values have been taken from ref 26 unless stated otherwise. [b] Ion $\Delta_f H$ taken from ref 69. [c] 1,2-Propadiene or allene.[69] [d] Propyne.[69] [e] Cyclopropene.[27] [f] Ion $\Delta_f H$ taken from ref 27.

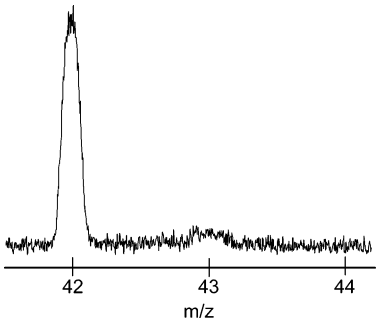

Figure 7. MIKES spectrum of metastable ionized acetone.

in the second field free region (2FFR), metastable acetone radical cations ($10^3 < k < 10^6$ s^{-1}, see Figure 8 where the fraction of acetone ions dissociating, dn/n_0, as a function of the rate constants has been inset) lose primarily methane with a trivial kinetic energy release of 2 meV, indicating that this reaction likely proceeds without a reverse activation barrier. Little, if any, methyl group loss is observed. Upon addition of a trace of He gas into the collision cell in the 2FFR (pressure reading on a nearby ion gauge of 1×10^{-8} mbar), a peak appears at *m/z* 43 due to methyl loss. This latter signal is very collision-sensitive, while the peak with *m/z* 42 is virtually insensitive to collision, meaning that any peak with *m/z* 43 discernible in Figure 7 is likely due to residual collisions with the background gas in the field free region. These results dictate the relative shapes and energies of the log $k(E)$ vs E curves for the two processes. There must be a very small internal energy window in which the total decay rate constant lies in the metastable regime, but in which methyl loss cannot compete with methane loss. In addition, the two competing $k(CH_3CO^+)$ and $k(CH_2CO^{+\bullet})$ curves cannot cross inside this internal energy window. Once the internal energy rises above the E_0 for methyl loss, $k(CH_3CO^+)$ rapidly increases above $k(CH_2CO^{+\bullet})$, and methyl loss dominates the mass spectrum. That the internal energy window is small is supported by the fact that metastable methane loss represents only 0.04% of the ion flux. Figure 8 shows that the theoretical RRKM curves produced in this study for $k(CH_3CO^+)$ and $k(CH_2CO^{+\bullet})$ are in good agreement with the above reasoning and with the experimental MIKES spectrum.

To estimate the 0 K activation energies for the two processes, RRKM modeling is required. The present study has approached the modeling of the breakdown diagram in a manner different to that used by Fogleman et al.[10] who summed together the molecular acetone ion and the ketene ion (*m/z* 42) signal in order to determine the onset for the acetyl ion (*m/z* 43). This summing of the parent and ketene ion intensities was carried out because the peak due to methane loss was observed to be metastable, while that for methyl loss was not. Hence, the former

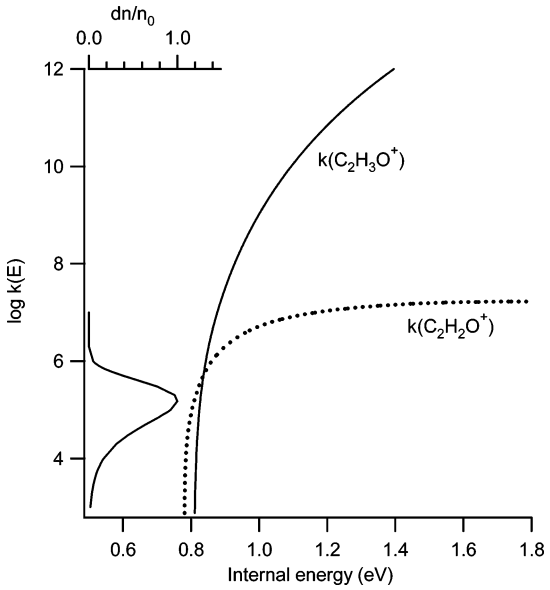

Figure 8. Log $k(E)$ vs E curves for the competing low-energy unimolecular dissociations of ionized acetone. Inset: the fraction of acetone ions dissociating, dn/n_0, by a first-order process in the 2FFR in the mass spectrometer as a function of the rate constants which lie between ca. 1×10^3 and 1×10^7 s^{-1}.

channel was assumed to originate from a long-lived precursor ion. For the two ions to be formed with different observed rate constants, they must originate from different precursors, a result inconsistent with the MIKES results presented above. Fogleman et al.[10] suggested isomerization to the enol isomer, but even if this occurred, it would result in methyl loss, not methane loss, due to the favorable kinetics for the former process at these high internal energies. The present study has examined the kinetics of the low-energy dissociations into $CH_2CO^{+\bullet}$ and CH_3CO^+ by modeling the breakdown diagrams in the threshold region. In the modeling procedure, the activation energy E_0 and the change in entropy of activation $\Delta S^{\ddagger}$ were treated as adjustable parameters and allowed to vary until a good fit was obtained between the theoretical convoluted curve and the experimental data at ion residences of 1.116 and 3.116 μs. The fitting yielded $E_0 = 0.81 \pm 0.020$ eV/78 ± 2 kJ mol^{-1} and $\Delta S^{\ddagger} = 87$ J K^{-1} mol^{-1} for the methyl loss channel, and $E_0 = 0.78 \pm 0.020$ eV/75 ± 2 kJ mol^{-1} and $\Delta S^{\ddagger} = -62$ J K^{-1} mol^{-1} for the methane loss channel. These results indicate that the transition state for the rearrangement to lose methane is much tighter than that for the more simple bond cleavage resulting in methyl loss, and yield log $k(E)$ vs E curves for the two channels consistent with the MIKES spectrum (Figure 8).

If, however, we assume an infinite rate for the methyl loss channel and model it as a step function, sum the methane loss channel and parent acetone ion together, and then convolute the curves with the ro-vibrational thermal energy distributions, we obtain an E_0 for methyl loss of 0.85 eV/82 kJ mol^{-1}. This can be considered identical to the E_0 of 0.855 ± 0.010 eV/83 kJ mol^{-1} derived by Fogleman et al.[10] Moreover, if we further convolute these breakdown curves, produced with the above step function, with our electron transmission function, we obtain a lower E_0 of 0.83 eV/80 kJ mol^{-1}, slightly higher than the E_0 derived from our RRKM fits.

The experimental E_0 values, combined with the IE of acetone of 9.708 eV, yield 0 K AEs for the formation of CH_3CO^+ and $CH_2CO^{+\bullet}$ of 10.52 ± 0.03 eV and 10.49 ± 0.03 eV, respectively. For methyl loss, the present result is in excellent agreement with values of 10.52 ± 0.02 eV and 10.49 ± 0.02 eV obtained from high-resolution photoionization efficiency curves measured in molecular beam studies using the hydrogen many-line spectrum[47] and synchrotron radiation,[6] respectively, as photon sources. However, it is noticeable that Wei et al.[6] report an AE for CH_3CO^+ which is lower than that for $CH_2CO^{+\bullet}$, contrary to the present results. This inversion may be due to a competitive shift, where the methane loss channel is suppressed by the extremely fast methyl loss channel. Our experimental results, in particular, the MIKES spectra where only methane loss is observed, dictate the relative shapes and energies of the log $k(E)$ vs E curves for the two processes (see Figure 8).

TABLE 8: Low-Energy Dissociation Thresholds

		dissociation thresholds[a]			
m/z	fragmention	literature values	CBS-APNO	G3	present result
43	CH_3CO^+	83 ± 1,[10] 77 ± 1[6]	81	72	78 ± 2
42	$CH_2CO^{+\bullet}$	82 ± 15,[10,26] 81 ± 2[6]	78	80	75 ± 2

[a] Values at 0 K in kJ mol^{-1}. Correction from 298 K employed calculated vibrational frequencies (see Table 3).

Ab Initio Modeling of the Low-Energy Dissociations. The overall potential energy surface shows that the acetone ion (**1**) can form two isomeric ion molecule complexes **2a** and **2b**. These two structures can then undergo simple bond cleavage to lose a methyl radical to form CH_3CO^+ without a barrier (Scheme 1). The higher-energy **2b** can rearrange via **TS1** to form the $CH_2CO^{+\bullet}/CH_4$ ion molecule complex **3** which undergoes cleavage to lose CH_4 and form $CH_2CO^{+\bullet}$. A key difference between the CBS-APNO[2] and G3 results is in the energy of **TS1**. CBS-APNO[2] predicts the energy to be below the dissociation products $CH_2CO^{+\bullet} + CH_4$, while G3 predicts the energy to be 5 kJ mol^{-1} above them.

The enthalpies of formation of the optimized species are shown in Table 3. The results are generally in very good agreement with literature values. However, closer inspection of the species related to the two low-energy dissociation channels shows that, while the 298 and 0 K values for methane and the 298 K values for CH_3CO^+ and $CH_2CO^{+\bullet}$ are in good agreement with the literature, the 0 and 298 K values for ionized acetone are ~5 kJ mol^{-1} too high and 6 kJ mol^{-1} too low, respectively, for neutral $CH_3^{\bullet}$. The calculated G3 $\Delta_f H(CH_3^{\bullet})$ value reported by Curtis et al.[25] is 5 kJ mol^{-1} too low compared to recent literature, in agreement with the present work. Due to these small discrepancies in the product ion and neutral G3 thermochemistry (Table 3), the product energies for $CH_3CO^+ + CH_3^{\bullet}$ and $CH_2CO^{+\bullet} + CH_4$ are inverted in comparison to the best experimental estimates and the CBS-APNO calculations. The MIKES result discussed earlier confirms that $CH_2CO^{+\bullet} + CH_4$ must lie lower in energy than $CH_3CO^+ + CH_3^{\bullet}$.

The RRKM fits to the experimental data yield E_0 values of 78 ± 2 kJ mol^{-1} for methyl loss and 75 ± 2 kJ mol^{-1} for methane loss, while the ab initio G3 calculations yield respective E_0 values of 72 and 80 kJ mol^{-1}. However, the value for the $CH_3^{\bullet}$ loss channel is expected to be 11 kJ mol^{-1} too low (see above). If we take this into account, the two different models still differ by 5 kJ mol^{-1} for both channels. Our E_0 value for $CH_3^{\bullet}$ loss is only 3 kJ mol^{-1} lower than the CBS-APNO thresholds calculated by Anand and Schlegel[2] (Table 8).

The present AEs of 10.52 ± 0.03 and 10.49 ± 0.03 eV, for the respective formation of the CH_3CO^+ and $CH_2CO^{+\bullet}$ ions, together with the well-established $\Delta_f H$ values for acetone, methane, and methyl radical (see Table 3) yield $\Delta_f H_0(CH_3CO^+) = 662 \pm 3$ kJ mol^{-1} and $\Delta_f H_0(CH_2CO^{+\bullet}) = 876 \pm 3$ kJ mol^{-1}.

After correcting to 298 K, the values are $\Delta_f H_{298}(CH_3CO^+) = 655 \pm 3$ kJ mol^{-1} and $\Delta_f H_{298}(CH_2CO^{+\bullet}) = 873 \pm 3$ kJ mol^{-1}. These values are in excellent agreement with those obtained by Traeger[30] using threshold photoionization mass spectrometry. The value for CH_3CO^+ is 4 kJ mol^{-1} lower than that obtained by Fogleman et al.,[10] and the discrepancy can be traced back to the different ways the breakdown diagrams were modeled. Summing the *m*/*z* 42 signal into the acetone ion signal resulted in a higher AE for the methyl loss channel (10.563 eV) than we obtained, and thus a slightly higher $\Delta_f H_{298}$ for CH_3CO^+. The fact that our result for the ketene ion agrees to within 4 kJ mol^{-1} of the accepted literature value indicates that the *m*/*z* 42 signal in the mass spectrum is likely the result of dissociation directly from ionized acetone and not from some other long-lived precursor ion. This is consistent with the tandem mass spectrometry of ionized acetone (see previous discussion and Figure 7). So, the present result suggests that the $\Delta_f H_{298}$ for CH_3CO^+ is closer to 655 ± 3 kJ mol^{-1} than 659.4 ± 1.1 kJ mol^{-1}. The present $\Delta_f H_{298}$ for CH_3CO^+ can be combined with the $\Delta_f H_{298}$ for CH_2CO (-47.5 ± 1.6 kJ mol^{-1})[50] and H^+ (1530 kJ mol^{-1}) to yield a 298 K proton affinity for ketene of 828 ± 4 kJ mol^{-1}, in good agreement with that calculated at the G2 level of theory by Smith and Radom[51] and listed in the NIST database (825 kJ mol^{-1}).[26]

Conclusion

The valence shell photoelectron spectrum of acetone has been measured at a photon energy of 80 eV, and the corresponding threshold photoelectron spectrum has also been recorded. A comparison between these two spectra has allowed the influence of resonant autoionization on the threshold photoelectron yield to be assessed. Autoionization from Rydberg series converging onto limits between ~12 and 17 eV significantly enhances the threshold photoelectron production and leads to two prominent broad structured peaks at ~14.2 and 15.6 eV. The same process also results in a finite yield in the Franck−Condon gap between the bands due to the $\tilde{X}\ ^2B_2$ and the $\tilde{A}\ ^2B_1$ states. New vibrational progressions have been observed and assigned in the $\tilde{X}\ ^2B_2$ state photoelectron bands of acetone-h_6 and acetone-d_6.

Kinetic modeling of the threshold region for the two low-energy dissociation channels has been performed. This modeling, which takes into account the ion residence time, the rovibrational population, the electron transmission efficiency, and the monochromator band-pass, has enabled theoretical breakdown curves to be calculated and compared with the corresponding experimental data. The fitting yields 0 K activation energies of 75 ± 2 and 78 ± 2 kJ mol^{-1} for CH_4 and $CH_3^\bullet$ loss, respectively. These E_0 values yield a $\Delta_f H_{298}$ for CH_3CO^+, 655 ± 3 kJ mol^{-1}, that is 4 kJ mol^{-1} lower than the 659.4 ± 1.1 kJ mol^{-1} reported by Fogleman et al.[10] The present $\Delta_f H_{298}$ for CH_3CO^+ can be combined with the $\Delta_f H_{298}$ for CH_2CO and H^+ to yield a 298 K proton affinity for ketene of 828 ± 4 kJ mol^{-1}.

Acknowledgment. The authors are grateful to the Council for the Central Laboratory of the Research Councils (UK) for the allocation of beamtime at the Daresbury Laboratory Synchrotron Radiation Source. P.M.M. thanks the Natural Sciences and Engineering Research Council of Canada for continuing financial support and the University of Ottawa for seed funds to undertake these experiments.

References and Notes

(1) McAdoo, D. J. *Mass Spectrom. Rev.* **2000**, *19*, 38.
(2) Anand, S.; Schlegel, H. B. *Phys. Chem. Chem. Phys.* **2004**, *6*, 5166.
(3) Nummela, J. A.; Carpenter, B. K. *J. Am. Chem. Soc.* **2002**, *124*, 8512.
(4) Heinrich, N.; Louage, F.; Lifshitz, C.; Schwarz, H. *J. Am. Chem. Soc.* **1988**, *110*, 8183.
(5) Ceño, M. D.; González-lafont, A.; Lluch, J. M.; Bertran, J. *Mol. Phys.* **1997**, *92*, 393.
(6) Wei, L.; Yang, B.; Yang, R.; Huang, C.; Wang, J.; Shan, X.; Sheg, L.; Zhang, Y.; Qi., F.; Lam, C.-S.; Li, W.-K. *J. Phys. Chem. A* **2005**, *109*, 4231.
(7) Lifshitz, C.; Tzidony, E. *Int. J. Mass Spectrom.* **1981**, *39*, 181.
(8) Osterheld, T. H.; Brauman, J. I. *J. Am. Chem. Soc.* **1992**, *114*, 7158.
(9) Stockbauer, R. *Int. J. Mass Spectrom.* **1977**, *25*, 89.
(10) Fogleman, E. A.; Koizumi, H.; Kercher, J. P.; Szta'ray, B.; Baer, T. *J. Phys. Chem. A* **2004**, *108*, 5288.
(11) Cant, C. S. T.; Danby, C. J.; Eland, J. H. D. *J. Chem. Soc., Faraday Trans. 2* **1975**, *71*, 1015.
(12) Mintz, D. M.; Baer, T. *Int. J. Mass Spectrom. Ion Phys.* **1977**, *25*, 39.
(13) Powis, I.; Danby, C. J. *Int. J. Mass Spectrom. Ion Processes* **1979**, *32*, 27.
(14) Johnson, K.; Powis, I.; Danby, C. J. *Chem. Phys.* **1981**, *63*, 1.
(15) Bombach, R.; Stadelmann, J. P.; Vogt, J. *Chem. Phys.* **1982**, *72*, 259.
(16) Holland, D. M. P.; Shaw, D. A.; Sumner, I.; Hayes, M. A.; Mackie, R. A.; Wannberg, B.; Shpinkova, L. G.; Rennie, E. E.; Cooper, L.; Johnson, C. A. F.; Parker, J. E. *Nucl. Instrum. Methods Phys. Res., Sect. B* **2001**, *179*, 436.
(17) Holland, D. M. P.; West, J. B.; MacDowell, A. A.; Munro, I. H.; Beckett, A. G. *Nucl. Instrum. Methods* **1989**, *B44*, 233.
(18) Keane, M. P.; Lunell, S.; Naves de Brito, A.; Carlsson-Göthe, M.; Svensson, S.; Wannberg, B.; Karlsson, L. *J. Electron Spectrosc. Relat. Phenom.* **1991**, *56*, 313.
(19) Holland, D. M. P.; MacDonald, M. A.; Hayes, M. A.; Baltzer, P.; Karlsson, L.; Lundqvist, M.; Wannberg, B.; von Niessen, W. *Chem. Phys.* **1994**, *188*, 317.
(20) Busch, K. L.; Glish, G. L.; McLuckey, S. A. *Mass Spectrometry/Mass Spectrometry*; VCH Publishers: New York, 1988.
(21) Holmes, J. L.; Mayer, P. M. *J. Phys. Chem. A* **1995**, *99*, 1366.
(22) Hehre, W. J.; Radom, L.; Schleyer, P. v. R.; Pople, J. A. *Ab Initio Molecular Orbital Theory*; Wiley: New York, 1986.
(23) Frisch, M. J.; Trucks, G. W.; Schlegel, H. B.; Scuseria, G. E.; Robb, M. A.; Cheeseman, J. R.; Zakrzewski, V. G.; Montgomery, J. A., Jr.; Stratmann, R. E.; Burant, J. C.; Dapprich, S.; Millam, J. M.; Daniels, A. D.; Kudin, K. N.; Strain, M. C.; Farkas, O.; Tomasi, J.; Barone, V.; Cossi, M.; Cammi, R.; Mennucci, B.; Pomelli, C.; Adamo, C.; Clifford, S.; Ochterski, J.; Petersson, G. A.; Ayala, P. Y.; Cui, Q.; Morokuma, K.; Malick, D. K.; Rabuck, A. D.; Raghavachari, K.; Foresman, J. B.; Cioslowski, J.; Ortiz, J. V.; Stefanov, B. B.; Liu, G.; Liashenko, A.; Piskorz, P.; Komaromi, I.; Gomperts, R.; Martin, R. L.; Fox, D. J.; Keith, T.; Al-Laham, M. A.; Peng, C. Y.; Nanayakkara, A.; Gonzalez, C.; Challacombe, M.; Gill, P. M. W.; Johnson, B. G.; Chen, W.; Wong, M. W.; Andres, J. L.; Head-Gordon, M.; Replogle, E. S.; Pople, J. A. *Gaussian 98*, revision A.6; Gaussian, Inc.: Pittsburgh, PA, 1998.
(24) Scott, A. P.; Radom, L. *J. Phys. Chem.* **1996**, *100*, 16502.
(25) Curtiss, L. A.; Raghavachari, K.; Refern, P. C.; Rassolov, V.; Pople, J. A. *J. Chem. Phys.* **1998**, *109*, 7764.
(26) *NIST Chemistry WebBook*; NIST Standard Reference Database Number 69; June 2005, Mallard, W. G., Linstrom, P. J., Eds.; National Institute of Standards and Technology: Gaithersburg, MD, http://webbook.nist.gov (accessed May 2006).
(27) Lias, S. G.; Bartmess, J. E.; Liebman, J. F.; Holmes, J. L.; Levin, R. D.; Mallard, W. G. *J. Phys. Chem. Ref. Data* **1988**, *17* (Supplement 1).
(28) Rennie, E. E.; Mayer, P. M. *J. Chem. Phys.* **2004**, *120*, 10561.
(29) Nicolaides, A.; Rauk, A.; Glukhovtsev, M. N.; Radom, L. *J. Phys. Chem.* **1996**, *100*, 17460.
(30) Traeger, J. C. *Int. J. Mass Spectrom.* **2000**, *194*, 261.
(31) von Niessen, W.; Schirmer, J.; Cederbaum, L. S. *Comput. Phys. Rep.* **1984**, *1*, 57.
(32) Baer, T.; Hase, W. L. *Unimolecular Reaction Dynamics, Theory and Experiments*; Oxford University Press: New York, 1996.
(33) Baer, T.; Mayer, P. M. *J. Am. Soc. Mass Spectrom.* **1997**, *8*, 103.
(34) Beyer, T.; Swinehart, D. R. *ACM Commun.* **1973**, *16*, 379.
(35) Brundle, C. R.; Robin, M. B.; Kuebler, N. A.; Basch, H. *J. Am. Chem. Soc.* **1972**, *94*, 1451.
(36) Tam, W.-C.; Yee, D.; Brion, C. E. *J. Electron Spectrosc. Relat. Phenom.* **1974**, *4*, 77.
(37) Kimura, K.; Katsumata, S.; Achiba, Y.; Yamazaki, T.; Iwata, S. *Handbook of He I Photoelectron Spectra of Fundamental Organic Molecules*; Japan Scientific Societies Press: Tokyo, 1981.
(38) McDiarmid, R. *J. Chem. Phys.* **1991**, *95*, 1530.
(39) Potts, A. W.; Williams, T. A.; Price, W. C. *Faraday Discuss. Chem. Soc.* **1972**, *54*, 104.

(40) Bieri, G.; Asbrink, L.; von Niessen, W. *J. Electron Spectrosc. Relat. Phenom.* **1982**, *27*, 129.
(41) Furuya, K.; Katsumata, S.; Kimura, K. *J. Electron Spectrosc. Relat. Phenom.* **1993**, *62*, 237.
(42) Zheng, Y.; Neville, J. J.; Brion, C. E.; Wang, Y.; Davidson, E. R. *Chem. Phys.* **1994**, *188*, 109.
(43) Thompson, D. B.; Ji, D.; Lee, K.; Ma, C.-I.; Hanson, D. M. *J. Phys. B* **1999**, *32*, 2649.
(44) Cederbaum, L. S.; Domcke, W.; Schirmer, J.; von Niessen, W. *Adv. Chem. Phys.* **1986**, *65*, 115.
(45) Merchan, M.; Roos, B. O.; McDiarmid, R.; Xing, X. *J. Chem. Phys.* **1996**, *104*, 1791.
(46) ter Steege, D. H. A.; Wirtz, A. C.; Buma, W. J. *J. Chem. Phys.* **2002**, *116*, 547.
(47) Trott, W. M.; Blais, N. C.; Walters, E. A. *J. Chem. Phys.* **1978**, *69*, 3150.
(48) Traeger, J. C.; Hudson, C. E.; McAdoo, D. J. *J. Phys. Chem.* **1988**, *92*, 1519.
(49) McAdoo, D. J.; Witiak, D. N. *J. Chem. Soc., Perkin Trans. 2* **1981**, 770.
(50) Pedley, J. B.; Naylor, R. D.; Kirby, S. P. *Thermochemical Data of Organic Compounds*, 2nd ed.; Chapman and Hall: New York, 1986.
(51) Smith, B. J.; Radom, L. *J. Am. Chem. Soc.* **1993**, *115*, 4885.
(52) Dorman, F. H. *J. Chem. Phys.* **1965**, *42*, 65.
(53) Johnstone, R. A. W.; Mellon, F. A.; Ward, S. D. *Int. J. Mass Spectrom. Ion Phys.* **1970**, *5*, 241.
(54) Johnstone, R. A. W.; Mellon, F. A. *J. Chem. Soc., Faraday Trans. 2* **1972**, *68*, 1209.
(55) Mouvier, G.; Hernandez, R. *Org. Mass Spectrom.* **1975**, *10*, 958.
(56) Staley, R. H.; Wieting, R. D.; Beauchamp, J. L. *J. Am. Chem. Soc.* **1977**, *99*, 5964.
(57) Murad, E.; Inghram, M. G. *J. Chem. Phys.* **1964**, *40*, 3263.
(58) Traeger, J. C.; McLouglin, R. G.; Nicholson, A. J. C. *J. Am. Chem. Soc.* **1982**, *104*, 5318.
(59) Potapov, V. K.; Sorokin, V. V. *Khim. Vys. Energ.* **1972**, *6*, 387.
(60) Potapov, V. K.; Filyugina, A. D.; Shigorin, D. N.; Ozerova, G. A. *Dokl. Akad. Nauk SSSR* **1968**, *180*, 398.
(61) Majer, J. R.; Olavesen, C.; Robb, J. C. *J. Chem. Soc. B* **1971**, 48.
(62) Shigorin, D. N.; Filyugina, A. D.; Potapov, V. K. *Teor. Eksp. Khim.* **1966**, *2*.
(63) Potapov, V. K.; Shigorin, D. N. *Zh. Fiz. Khim.* **1966**, *40*, 200.
(64) Stadelmann, J. P. *Chem. Phys. Lett.* **1982**, *89*, 174.
(65) Potzinger, P.; Bunau, G. v. *Ber. Bunsen-Ges. Phys. Chem.* **1969**, *73*, 466.
(66) Haney, M. A.; Franklin, J. L. *J. Chem. Soc., Faraday Trans.* **1969**, *65*, 1794.
(67) Kanomata, I. *Bull. Chem. Soc. Jpn.* **1961**, *34*, 1864.
(68) Wiedmann, R. T.; Goodman, L.; White, M. G. *Chem. Phys. Lett.* **1998**, *293*, 391.
(69) *NIST Standard Reference Database 25*; National Institute of Standards and Technology: Gaithersburg, MD, 1994.